scientific reports

OPEN

Defected ground structure antenna array with metasurface inspired interlinked CSRR for 5G millimeter wave applications

Esraa Mousa Ali[1], Mohammad Alibakhshikenari[2,3]✉, Nouf Abd Elmunim[4]✉, Bal S. Virdee[5], Nasr Rashid[6,7], Dion Mariyanayagam[5], Muhammad Akmal Chaudhary[8], Nisar Ahmad Abbasi[9], Patrizia Livreri[10]✉ & Takfarinas Saber[2]

This paper introduces a high-performance antenna array optimized for 5G millimeter-wave (mm-Wave) applications, efficiently operating within the 25–30 GHz frequency range. Three integrated techniques enhance performance without increasing physical size: First, a Defected Ground Structure (DGS) with a 25 × 25 mm² square slot and embedded interlinked complementary split-ring resonators (CSRRs) inspired by metasurface (MTS) principles broaden bandwidth and improve impedance matching. Second, four oblique slots (4.5 × 0.4 mm²) placed at the ground plane's corners enhance impedance matching, isolation, and extend the upper frequency to 30 GHz. Third, slotted radiation patches optimize radiation gain and efficiency. Initially, the design operated at 26.0–26.5 GHz and 27.5–28.0 GHz with a radiation gain of 2.8 dBi and efficiency of 56%. Incorporating DGS with CSRRs expanded bandwidth to 25–30 GHz, increased average radiation gain to 7.75 dBi, and improved efficiency to 68.75%. Introducing oblique slots further elevated the average gain to 9.15 dBi and efficiency to 79.5%. Finally, integrating open-loop slots into radiating patches raised the average gain to 12.4 dBi and efficiency to 86.25%. The final optimized antenna array, measuring 32 × 32 × 0.8 mm³, demonstrates significant improvements in radiation gain and efficiency, making it a compact, lightweight, cost-effective, and practical solution for 5G and other mm-Wave applications.

The rapid advancement of wireless networking technologies has driven an increasing demand for higher bandwidth and data rates, fuelled by the proliferation of smart devices and emerging applications[1–3]. However, the frequency range below 6 GHz, which has traditionally supported cellular networks, is becoming increasingly congested[4]. To overcome this limitation, millimeter-wave (mm-Wave) bands have been identified as a key enabler for fifth generation (5G) networks, offering significantly wider bandwidths capable of supporting multi-gigabit-per-second data rates[5,6]. As a result, mm-Wave technology has garnered considerable attention from both researchers and industry as a fundamental component of next-generation 5G mobile communications[7–9].

[1]Communications and Computer Engineering Department, Al-Ahliyya Amman University, Amman 19111, Jordan. [2]Lero, the Research Ireland Centre for Software, School of Computer Science, University of Galway, Galway H91 TK33, Ireland. [3]Department of Electrical and Electronics Engineering, Dogus University, 34775 Umraniye, Istanbul, Türkiye. [4]Department of Electrical Engineering, College of Engineering, Princess Nourah bint Abdulrahman University, P.O. Box 84428, Riyadh 11671, Saudi Arabia. [5]Center for Communications Technology, School of Computing and Digital Media, London Metropolitan University, London N7 8DB, UK. [6]Electrical Engineering Department, College of Engineering, Jouf University, Sakaka 72388, Aljouf, Saudi Arabia. [7]Department of Electrical Engineering, Faculty of Engineering, Al-Azhar University, Nasr City 11884, Cairo, Egypt. [8]Department of Electrical and Computer Engineering, Ajman University, Ajman, UAE. [9]Department of Electrical Engineering, University of Hafr Al Batin, Hafr Al Batin 39524, Saudi Arabia. [10]Department of Engineering, University of Palermo, Palermo 90128, Italy. ✉email: mohammad.alibakhshikenari@universityofgalway.ie; naasmail@pnu.edu.sa; patrizia.livreri@unipa.it

Despite its advantages, the transition from traditional sub-6 GHz frequencies to mm-Wave bands presents several technical challenges, including high free-space path loss and signal blockage in non-line-of-sight conditions. To address these issues, high-gain, narrow-beam antennas with beamforming capabilities are essential[10]. Phased antenna arrays, which enable beam steering by dynamically adjusting phase shifts, play a crucial role in maintaining reliable communication links in 5G mm-Wave networks[11,12].

However, designing antenna arrays that simultaneously achieve wide bandwidth, high gain, and compact size remains a significant challenge. Atmospheric absorption and signal attenuation at higher frequencies, particularly at 28 GHz, a key 5G band, further complicate antenna design[4]. Various antenna architectures have been explored to mitigate these issues, but many existing solutions face trade-offs in terms of bandwidth, gain, or fabrication complexity.

For instance, a phased array design for 5G mobile communications in[13] employed a ten-slot loop antenna on an FR-4 substrate, achieving 13 dBi gain over 27–29 GHz. However, FR-4 exhibits significant losses at mm-Wave frequencies, limiting overall efficiency. Similarly, in[14], a planar antipodal Fermi tapered slot array covering 27–32 GHz utilized metamaterial corrugations to reduce mutual coupling and enhance bandwidth, achieving 15 dBi gain. However, its complex structure requires precise fabrication, making large-scale implementation challenging. In[15], three patch antenna arrays were designed for the 28 GHz band, using printed circuit board (PCB) and low-temperature co-fired ceramic (LTCC) substrates. While the PCB-based array achieved 13 dBi gain and the LTCC-based array reached 10 dBi, both suffered from limited bandwidth.

To address mm-Wave design challenges, some researchers have adopted substrate integrated waveguide (SIW) technology, as demonstrated in[16], where a slotted rectangular SIW-based antenna achieved 13.8 dBi gain and 92% efficiency over 28–36 GHz. Although SIW designs offer high gain and low cost, they introduce complex manufacturing constraints. Similarly, dielectric resonator antennas (DRAs) have been explored for mm-Wave applications, as in[17], where a 1×4 DRA linear array achieved 14 dBi gain with a 2.1 GHz bandwidth. However, DRAs present challenges in scalability and integration with other circuit components.

Despite these advancements, the trade-offs between gain, bandwidth, design complexity, and fabrication feasibility remain unresolved in many existing solutions. Achieving an optimal balance of high gain, wide bandwidth, and compact size is still an open research challenge in 5G mm-Wave antenna design.

In this work, we propose a compact, high-performance 2×2 MIMO antenna array that effectively overcomes these limitations by integrating Defected Ground Structures (DGS) with Complementary Split-Ring Resonators (CSRRs), slot loading techniques, and metasurface (MTS) concepts. These design enhancements significantly reduce substrate losses, suppress surface waves, and expand the effective aperture area without increasing the physical size of the antenna. The proposed $32 \times 32 \times 0.8$ mm^3 array, fabricated on a Rogers RT5880 substrate, operates efficiently across the 25–30 GHz frequency range, with resonance points at 26.0 GHz and 28.25 GHz. It achieves an average radiation gain of more than 12.5 dBi and efficiency above 85%, while providing excellent impedance matching (>40 dB) and inter-element isolation (>35 dB) at both resonance frequencies. These improvements demonstrate that the proposed design offers a competitive solution, surpassing many existing approaches in terms of bandwidth, gain, isolation, and overall efficiency for 5G mm-Wave communication systems.

Furthermore, the proposed antenna remains lightweight, cost-effective, and suitable for large-scale production, making it a promising candidate for integration into next generation 5G wireless devices and networks.

Antenna array realization

The design of the antenna array began with the selection of the Rogers RT5880 substrate, chosen for its favorable electromagnetic properties, including a dielectric constant ($\varepsilon_r = 2.2$), a low loss tangent (tan$\delta = 0.0009$), and a thickness of 0.8 mm, making it well-suited for millimeter-wave (mm-Wave) applications. The array consists of four radiating elements arranged in a square configuration; each composed of three interconnected patches in a three-petal shape. This configuration was specifically chosen to enhance radiation characteristics and improve the overall antenna performance.

The radiating patches are excited using microstrip feedlines, which generate a quasi-TEM mode, ensuring efficient energy transfer to the radiating elements. The symmetrical structure of the radiating elements facilitates a uniform field distribution, reducing impedance mismatches and enhancing radiation efficiency. Additionally, the ground plane acts as a reflective surface, reinforcing radiation in the forward direction and further optimizing antenna performance.

The four radiating elements are positioned on the same side of a common substrate, with opposite elements arranged symmetrically, as illustrated in Fig. 1a. This configuration significantly enhances the array's gain and directivity, which are crucial for mitigating signal losses at mm-Wave frequencies. Furthermore, this arrangement improves beamforming capabilities, enhances inter-element isolation, and increases overall efficiency, as demonstrated in later analyses.

The primary objective of this design was to develop an antenna array capable of covering the 25–30 GHz frequency range, which is essential for 5G mm-Wave applications. A prototype of the initial design, featuring a fully grounded plane as shown in Fig. 1b and compact dimensions of $32 \times 32 \times 0.8$ mm^3, was fabricated and evaluated. The dimensions of the antenna array are listed in Table 1.

The S-parameter analysis, shown in Fig. 1c, revealed that the array operated in two frequency bands: 26.0–26.5 GHz and 27.5–28.0 GHz, each with a 0.5 GHz bandwidth, aligning with the operational requirements of 5G networks. The array exhibited fractional bandwidths of 1.9% and 1.8% at resonances of 26.25 GHz and 27.75 GHz, with impedance matching values of -19 dB and -12 dB, respectively.

Inter-element isolation was a critical design consideration to minimize interference. The measured average isolation between antenna elements was -8 dB (S_{12}), -12 dB (S_{13}), and -10 dB (S_{14}), ensuring sufficient
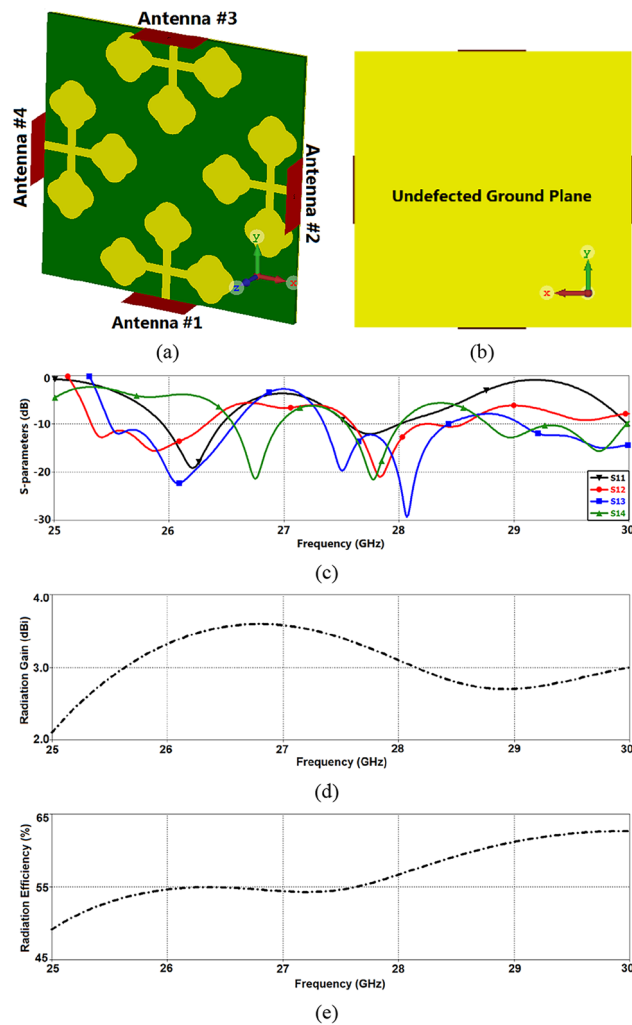
Fig. 1. Basic array antenna model #1, (**a**) top view, (**b**) bottom view, (**c**) S-parameter responses, (**d**) radiation gain response, and (e) radiation efficiency performance. The figures and the plots have been generated by the CST Microwave Studio version 2024 as a 3D full-wave electromagnetic software. Software link: https://www.3d s.com/products/simulia/cst-studio-suite[18].

separation to reduce unwanted coupling. The radiation characteristics, presented in Fig. 1d,e, indicate that the array achieved gains between 2.1 dBi and 3.6 dBi, with efficiencies ranging from 49 to 63% over 25 GHz to 30 GHz. The average gain and efficiency across the operating bands were 3.25 dBi and 57.5%, respectively.

The design process and performance evaluations were conducted using Computer Simulation Technology (CST) Microwave Studio, employing the finite-difference time-domain (FDTD) method to ensure accurate simulations within the targeted frequency range. The results confirm the effectiveness of the proposed design for 5G mm-Wave applications.

To enhance the frequency bandwidth and improve the performance parameters of the initial antenna array (#1) while maintaining its physical dimensions, three simple yet effective modifications were implemented:

1. Printed slots and a complementary split-ring resonator (CSRR)-inspired metasurface were incorporated to reduce substrate losses and enhance bandwidth.
2. Angled slots were introduced to improve impedance matching and further increase bandwidth.
3. Additional slots in the radiating patches were implemented to fine-tune radiation characteristics and extend the operational range.

These modifications enabled the proposed array antenna to operate efficiently across the full 25–30 GHz 5G band, while simultaneously achieving high isolation between radiating elements and enhanced radiation properties. The subsequent sections provide a detailed discussion of these design enhancements.

Slot and CSRR loaded antenna array
In the array design, a 25×25 mm^2 square slot was etched onto the ground plane and loaded with an array of interlinked Complementary Split-Ring Resonators (CSRRs) inspired by the metasurface (MTS) concept, as

Size	$32 \times 32 \times 0.8$ mm^3
Substrate	Rogers RT 5880, $\epsilon_r = 2.2$, tang $\delta = 0.0009$, $h = 0.8$ mm
r_1	3 mm
r_2	2 mm
w	0.25 mm
l_f	4 mm
w_f	1 mm
l_c	6 mm
w_c	1 mm
L	32 mm
W	3.5 mm
Ls	25 mm
Ws	25 mm
l_{ob}	4.5 mm
w_{ob}	0.4 mm
θ	45°
Number of the CSRR's ring	3
w_{cssr}	0.25 mm
g	0.25 mm
w_{slot}	0.25 mm
d_3	1.5 mm
d_2	1 mm
d_1	0.5 mm

Table 1. Geometrical parameters of the proposed array antenna.

illustrated in Fig. 2a[19]. The top side of the substrate accommodated the four radiating elements, as shown in Fig. 1a.

Figure 2b depicts the layout of the interlinked CSRR structure. When excited by incident RF energy, this configuration exhibits resonance, leading to effective negative permittivity and permeability within specific frequency ranges. The conductive paths within the resonator structure function as left-handed (LH) inductive elements (L_L), while the capacitive coupling between the gaps of the rings generates left-handed capacitances (C_L). The combined values of these inductances and capacitances determine the resonance frequency, which ultimately governs the electromagnetic response of the structure[19].

The equivalent circuit model of the CSRR unit cell, depicted in Fig. 2c, further illustrates this behavior. The electromagnetic resonance frequency of the CSRR is primarily influenced by the magnitudes of L_L and C_L. Mathematically, the resonance frequency can be expressed as[20]:

$$f = \frac{1}{\pi \sqrt{C_L L_L}} \tag{1}$$

This equation highlights the dependency of the structure's electromagnetic response on its physical geometry and material composition.

The capacitance between the splits is defined by the following expression:

$$C(F) = \epsilon_0 \epsilon_r \frac{g}{L} \tag{2}$$

where, ϵ_0, ϵ_r, g, and L denote free space and relative permittivity, area of the split, and the split length, respectively. The equivalent inductance is computed based on the transmission-line concept given by[21]:

$$L(nH) = 2 \times 10^{-4} l \left[ln\left(\frac{l}{w+t}\right) \right] + 1.193 + 0.02235 \left(\frac{w+t}{l}\right) \left[0.57 - 0.145\, ln\left(\frac{w'}{h'}\right) \right] \tag{3}$$

In this context, l, w, and t represent the length, width, and thickness of the microstrip line, respectively. The variables w' and h' denote the thickness and width of the substrate, respectively. To determine the total inductance, both the external and internal inductances must be calculated.

The CSRRs, etched into the defected ground structure, are excited when RF energy from the microstrip-fed patches couples through the ground plane. The CSRRs act as resonators, generating negative permittivity and permeability in specific frequency bands. The incident RF energy originates from the radiating patches located on the top layer of the substrate. Since the CSRRs are in the ground plane, energy couples from the microstrip-fed radiating elements to the CSRR structures, leading to the observed resonance. The radiating patches on the top layer generate the primary RF signal. Some of this energy couples downwards through the substrate and interacts
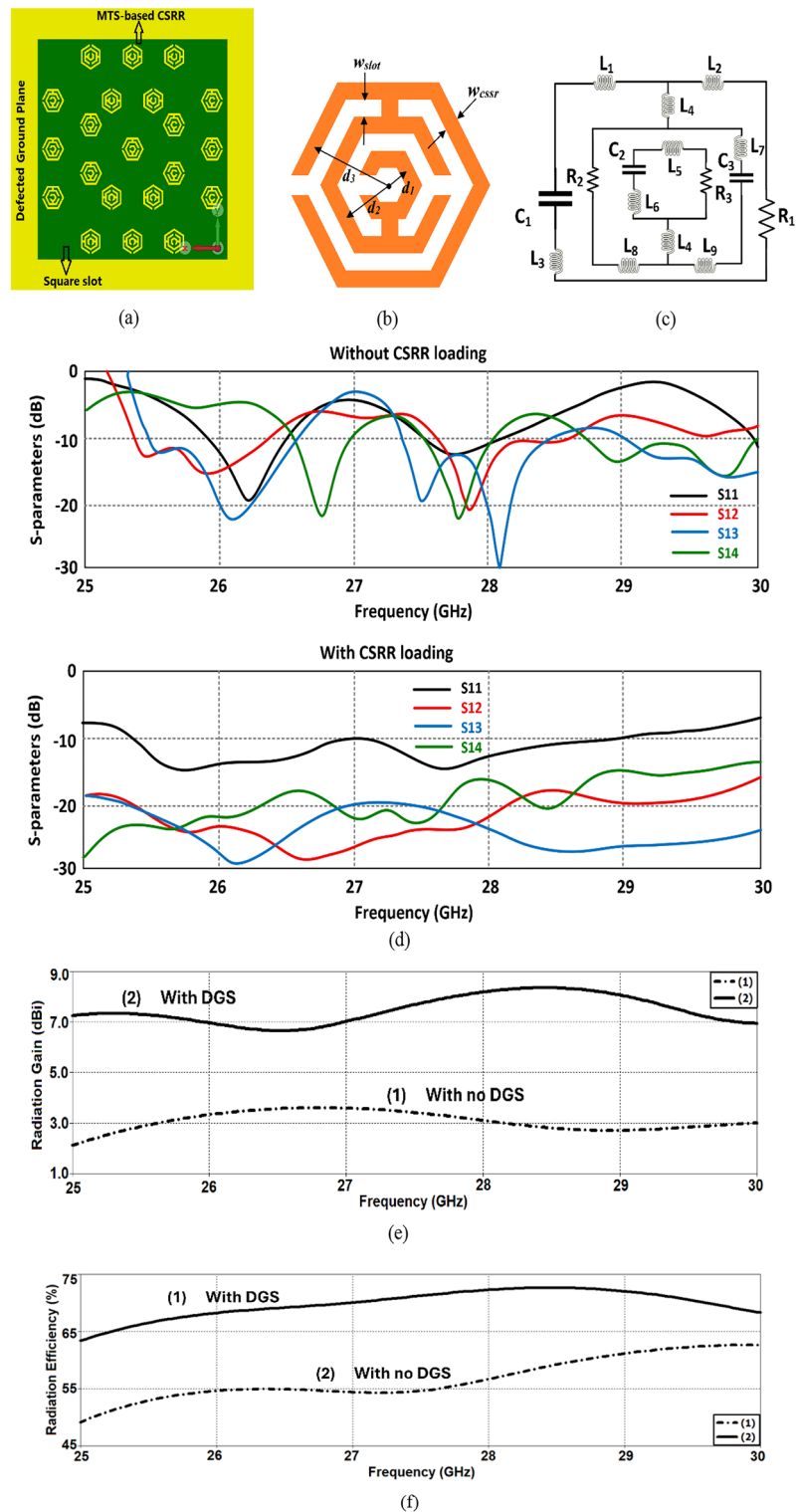
Fig. 2. (**a**) Basic array antennas with a defected ground plane (DGP) that includes a square slot loaded with metasurface (MTS)-based complementary split ring resonators (CSRR). The top side of the antenna remains unchanged and is similar to Fig. 1a. (**b**) MTS-based CSRR unit cell. (**c**) Equivalent circuit model of the SRR unit cell. (**d**) Comparison of the S-parameter responses for the first (1) and second (2) array antennas before and after applying DGS constructed by MTS-based CSRR loading. (**e**) Comparison of radiation properties, including gain, and (**f**) efficiency. Please note that, due to the symmetric nature of the array layout (i.e., $S_{11} = S_{22} = S_{33} = S_{44}$), only S_{11}, S_{12}, S_{13}, and S_{14} are presented to avoid unnecessary information. The figures and the plots have been generated by the CST Microwave Studio version 2024 as a 3D full-wave electromagnetic software. Software link: https://www.3ds.com/products/simulia/cst-studio-suite[18].

with the CSRR structures on the ground plane. The coupled energy excites the CSRRs, modifying the effective impedance and resonance characteristics of the antenna. The CSRR is designed to resonate primarily around 28 GHz in this study. Also, the CSRR arrangement was determined based on electromagnetic optimization rather than periodicity. Their count and positioning were selected through a combination of simulation-driven analysis, resonance tuning, and impedance matching.

The S-parameter response of the proposed antenna array is illustrated in Fig. 2d. The response without CSRR loading is demonstrated as top figure, while the response with CSRR loading is depicted as bottom figure. The reflection coefficients for both configurations vary across the frequency range, with CSRR-loaded ports exhibiting deeper resonance dips, particularly around 28 GHz. This indicates enhanced impedance matching and stronger resonances due to the introduction of CSRRs.

The transmission coefficients between ports show distinct variations depending on the presence of CSRR loading. Specifically, S_{12} and S_{13} for CSRR-loaded exhibit sharper and more pronounced attenuation in specific frequency bands compared to S_{12} and S_{13} without CSRRs loading. This suggests that CSRR loading modifies the coupling between ports, leading to selective frequency filtering or suppression, particularly around 28 GHz.

Furthermore, the coupling coefficient is significantly lower for CSRR-loaded antenna (S_{14}) across much of the frequency range. This indicates that CSRRs effectively reduce unwanted coupling between distant ports, thereby enhancing isolation. Improved isolation is critical in multi-port antenna systems to minimize interference and optimize overall performance.

Additionally, CSRR-loaded antenna introduces pronounced frequency-dependent behavior in the transmission coefficients (S_{12}, S_{13}), demonstrating their ability to function as frequency-selective structures. The sharper resonance dips observed in the reflection coefficients (S_{11}, S_{22}) highlight enhanced impedance control at specific frequencies. The leftward shift of S_{13} relative to S_{14} is primarily attributed to the increased effective capacitance and inductance introduced by the CSRRs.

In this design, the interlinked CSRR structures act as metamaterial inclusions that induce negative effective permittivity and permeability within specific frequency bands. These CSRRs behave like resonant *LC* circuits, where the metallic rings and gaps introduce series inductance and capacitance. When excited by incident RF signals, they generate left-handed (LH) properties, leading to backward wave propagation. This phenomenon enhances the electromagnetic response of the antenna by concentrating the electric field around the resonators, which improves resonance sharpness and increases the effective impedance control. Additionally, these effects broaden the operational bandwidth and create stronger resonance notches, which are critical for high-gain antenna design. The induced electromagnetic behavior also leads to field confinement in the vicinity of the ground plane, which minimizes energy leakage and surface wave propagation.

Overall, the inclusion of CSRRs in the antenna array significantly enhances its electromagnetic response, leading to sharper resonances, improved isolation, and greater frequency selectivity. These effects are evident in the lower transmission levels and deeper reflection dips observed for CSRR-loaded ports. As a result, the CSRR-loaded design is well-suited for applications requiring precise control over electromagnetic behavior in the 25–30 GHz frequency range.

The radiation gain of the 4-port antenna array, as shown in Fig. 2e, compares the performance of the design without DGS (no CSRR loading) and with DGS (CSRR loading) across the 25–30 GHz frequency range. In the absence of CSRR loading, the gain remains relatively low, fluctuating around 3 dBi throughout the frequency range. This indicates that the antenna design without CSRR loading is less efficient in radiating RF energy into free space. In contrast, with CSRR loading, the gain is significantly higher, ranging from 6.5 dBi to 8.5 dBi, with a peak at approximately 28.5 GHz. This substantial improvement in radiation gain demonstrates the effectiveness of CSRR loading in enhancing the antenna's ability to efficiently radiate RF energy.

Similarly, as demonstrated by Fig. 2f the radiation efficiency without CSRR loading remains low across the frequency range, starting at 49% at 25 GHz and increasing slightly to 64% at 30 GHz. This suggests that significant energy is lost due to factors such as impedance mismatch, material losses, or coupling effects. However, with CSRR loading, the efficiency is notably improved, beginning at 64% at 25 GHz, reaching a peak of approximately 73% at 28.5 GHz, and then slightly decreasing to 68% at 30 GHz. This efficiency enhancement highlights the role of CSRRs in reducing losses and improving energy transfer to free-space radiation.

The CSRR-loaded configuration significantly enhances both radiation gain and efficiency compared to the non-CSRR-loaded design. The gain increases by approximately 6 dBi, while efficiency improves by 10–15% across the entire frequency range. These improvements are particularly pronounced at 28.5 GHz, making CSRR-loaded antenna arrays highly suitable for applications that require high-performance radiation characteristics in this frequency band.

Antenna array with DGS oblique slot loading

The next objective in the study was to enhance the impedance matching of the antenna array without altering its physical dimensions or degrading its performance characteristics. To achieve this, four oblique slots, each measuring 4.5×0.4 mm^2, were introduced at the corners of the DGS, as shown in Fig. 3a. The slot dimensions were optimized using CST Microwave Studio to maximize performance. The S-parameter responses of the antenna array are illustrated in Fig. 3b for three configurations: (1) without DGS (no CSRR loading), (2) with DGS (CSRR loading), and (3) with DGS (CSRR loading) and oblique slots.

The impedance matching characteristics vary across these configurations. In the absence of CSRR loading (S_{11}), the resonance dips are shallow, indicating weaker impedance matching. When CSRR loading is introduced (S_{11}), the resonance dips become deeper and sharper, particularly around 27.5–28 GHz, demonstrating enhanced impedance matching and resonance behavior. The DGS oblique slots configuration (S_{11}) exhibits the deepest reflection dips across the entire frequency range, suggesting optimal impedance matching due to the additional tuning effect of the DGS structure.
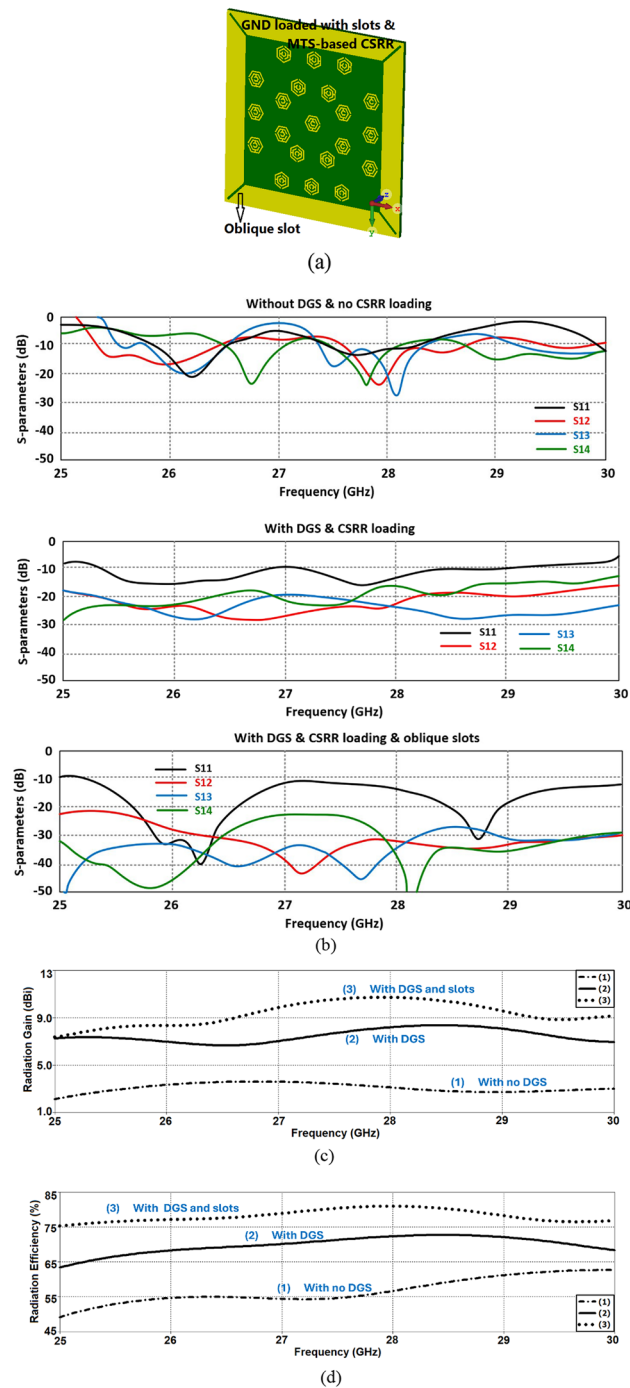
(a)

(b)

(c)

(d)

Fig. 3. (**a**) Basic array antennas with defected ground plane (DGP) loaded with (i) a square slot containing the metasurface (MTS) based complementary split ring resonators (CSRR), and (ii) four oblique slots located on corners. The topside of the antenna is unchanged and similar with Fig. 1a. (**b**) Comparison of the S-parameter responses of the first array antenna without DGS and CSRR loading, second array antenna with DGS and CSRR loading, and third array antenna with DGS and CSRR loading and oblique slots. Comparison of the radiation properties of these antennas in terms of (**c**) gain, and (**d**) radiation efficiency. Please note that, since the array layout is symmetric, i.e., $S_{11} = S_{22} = S_{33} = S_{44}$, only S_{11}, S_{12}, S_{13}, and S_{14} have presented to prevent unnecessary crowding. The figures and the plots have been generated by the CST Microwave Studio version 2024 as a 3D full-wave electromagnetic software. Software link: https://www.3ds.com/products/simulia/cst-studio-suite[18].

Similarly, the transmission coefficients indicate differences in coupling behavior among the configurations. The antenna without CSRR loading exhibit higher transmission magnitudes, implying stronger coupling between ports, which can lead to interference. With CSRR loading, notable attenuation is observed in specific frequency bands, particularly around 28 GHz, demonstrating the ability to reduce coupling and enable selective frequency filtering. The DGS oblique slots configuration further reduces coupling across the entire frequency range, as evidenced by the lower transmission coefficients compared to the other two configurations. This confirms that DGS enhances isolation and minimizes unwanted interactions between ports, significantly improving antenna performance.

The impact of CSRR loading and DGS oblique slots on radiation gain and efficiency is illustrated in Figs. 3(c) and 3(d). The gain performance of the antenna array varies significantly depending on the configuration. Without CSRR loading (S_{11}), the gain remains low, fluctuating between 2 and 3 dBi across the 25–30 GHz frequency range, indicating suboptimal radiation performance. In contrast, with CSRR loading, the gain improves significantly, ranging between 7 and 8 dBi, with a slight peak around 28 GHz. This demonstrates the effectiveness of CSRRs in enhancing radiation by improving impedance matching and reducing losses. Notably, the DGS oblique slots configuration achieves the highest radiation gain, peaking above 11.3 dBi around 28 GHz. This configuration consistently outperforms the others across the frequency range, confirming the superior radiation performance enabled by the combination of CSRR loading and DGS design.

The radiation efficiency also varies significantly across configurations. Without CSRR loading, the efficiency starts at 47% at 25 GHz and increases gradually to 63% at 30 GHz, suggesting higher energy losses in this configuration. The CSRR-loaded antenna array exhibits a notable improvement, with efficiency starting at 64% at 25 GHz and peaking at 74% around 28 GHz. The DGS oblique slots configuration further enhances radiation efficiency, starting at 75% at 25 GHz and exceeding 80% around 28 GHz, maintaining superior performance across the entire frequency range. The improved efficiency indicates reduced energy losses and better utilization of input power for radiation, making this design highly efficient.

The oblique slots introduced into the DGS alter the surface current distribution across the ground plane. These diagonally oriented slots act as reactive loading elements that interrupt and re-route the current paths. This redirection creates multiple current loops that contribute to more uniform radiation and reduced surface wave losses. As a result, the antenna exhibits improved impedance matching across a wider bandwidth. The presence of these slots also enhances inter-element isolation by suppressing mutual coupling between adjacent ports. This decoupling effect is particularly beneficial in MIMO configurations, where strong isolation ensures better signal diversity and reduced interference. Overall, the slots contribute to higher radiation efficiency and stable gain by improving current flow symmetry and minimizing reflective losses.

Overall, the results clearly demonstrate the effectiveness of CSRR loading and DGS oblique slots in enhancing the radiation performance of the antenna array. While CSRRs alone significantly improve gain and efficiency, the addition of DGS oblique slots achieves the highest gain (above 10 dBi) and efficiency (over 80%), making it the optimal design for applications requiring high-performance antennas in the 25–30 GHz frequency range.

DGS antenna array with slot loaded patches

The next objective in the study was to enhance the performance of the 2×2 antenna array for 5G mm-Wave applications within the 25–30 GHz frequency range, without increasing its physical dimensions of 32×32×0.8 mm^3. To achieve this, each radiating element in the array was loaded with an open-loop slot, as shown in Fig. 4a. The slot profile follows the periphery of the petal-shaped patch, effectively expanding the aperture of the antenna. As demonstrated in later sections, this technique significantly enhances the array's radiation properties, including radiation gain and efficiency, while also improving impedance bandwidth and inter-element isolation. The antenna array dimensions are provided in Table 1.

The configuration of the proposed antenna array with DGS and slot-loaded patches is illustrated in Fig. 4a–d. Since standard SMA connectors are only applicable up to 18 GHz, precision SMA connectors with extended capabilities up to 30 GHz were used in this study to ensure accurate measurements.

The S-parameter response of the 4-port antenna array, shown in Fig. 4e, provides key performance metrics across the 25–30 GHz frequency range. The curves represent various reflection and transmission coefficients, where the top figure refers to the array without slot-loaded radiation patches, and the bottom one corresponds to the array with slot-loaded radiation patches. The S_{11} parameter, representing reflection at Port 1, is shown by the black curves. The array without slot-loaded radiation patches indicates higher reflection levels compared to the slot-loaded array, which exhibits lower reflection, demonstrating improved impedance matching due to slot-loading. Similarly, S_{12}, S_{13}, and S_{14}, represented by the red, blue, and green curves, respectively, depict inter-port coupling. These curves show noticeable frequency-dependent variations, reflecting the influence of slot-loading on reducing inter-port coupling. Overall, the slot-loaded antenna array exhibits lower reflection and improved inter-port isolation, as evident from smoother and reduced S-parameter levels, particularly in key reflection and transmission characteristics.

The radiation gain and efficiency characteristics of the slot-loaded 4-port antenna array are depicted in Fig. 4f, g, comparing experimental and simulation results. In Fig. 4f, the simulated radiation gain remains stable and slightly higher across the frequency range, following a consistent trend. The experimental gain closely follows the simulation, though minor variations and a slight reduction in gain are observed, potentially due to fabrication tolerances, measurement setup, or environmental factors. The peak radiation gain is 14 dBi at 27.25 GHz, while the average measured radiation gain across 25–30 GHz is 12.4 dBi.

The achieved radiation gain of 12.4 dBi results from a combination of three techniques. First, the defected ground structure with interlinked CSRRs increases the effective aperture and suppresses surface wave losses. Second, the oblique slots improve impedance matching and inter-element isolation, ensuring efficient power
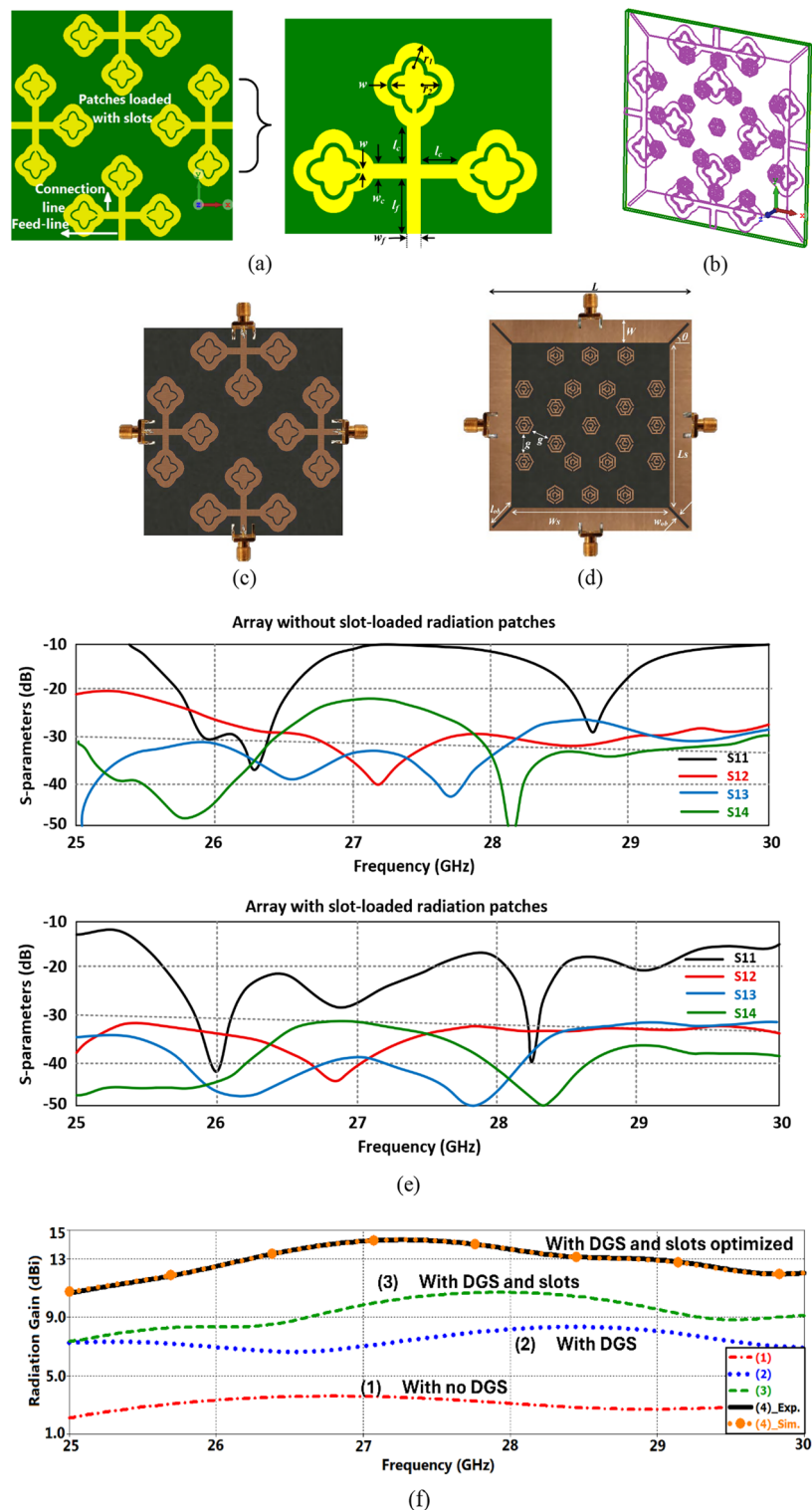
Fig. 4. The optimized array antenna with DGS loaded with CSRRs and diagonal slots, (**a**) Top view of the simulated layout, (**b**) Schematic view of the simulated layout, (**c**) Top view of the fabricated prototype antenna, (**d**) Back view of the fabricated prototype antenna, (**e**) simulated and measured S-parameter responses between the ports, (**f**) simulated and measured radiation gain, (**g**) simulated and measured radiation efficiency, (**h**) Radiation measurement setup, (**i**) simulated and measured radiation patterns in the E-plane at 26.0 GHz, and (**j**) simulated and measured radiation patterns in the H-plane at 28.25 GHz. The figures and the simulated plots have been generated by the CST Microwave Studio version 2024 as a 3D full-wave electromagnetic software. Software link: https://www.3ds.com/products/simulia/cst-studio-suite[18].
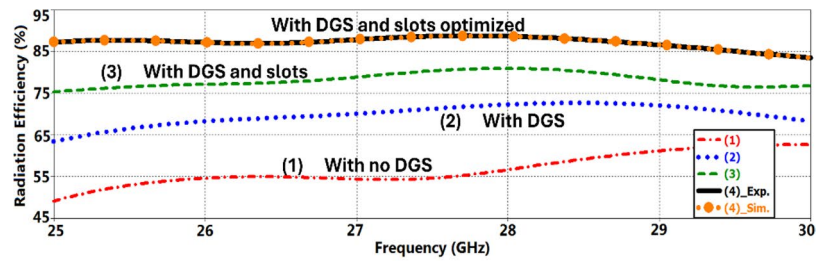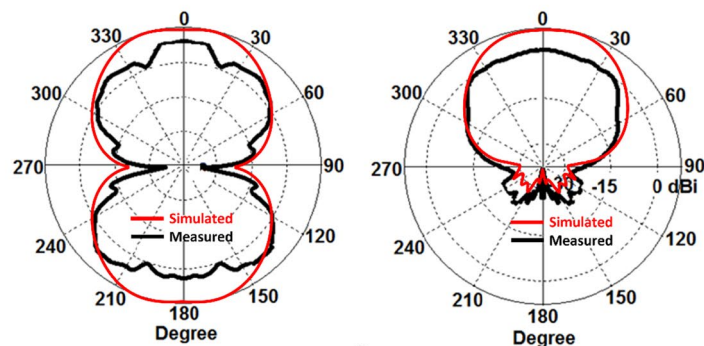
(g)
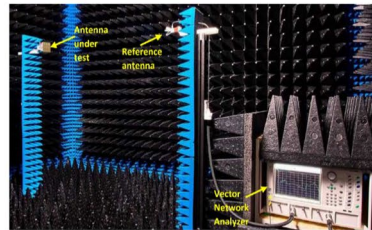
(h)
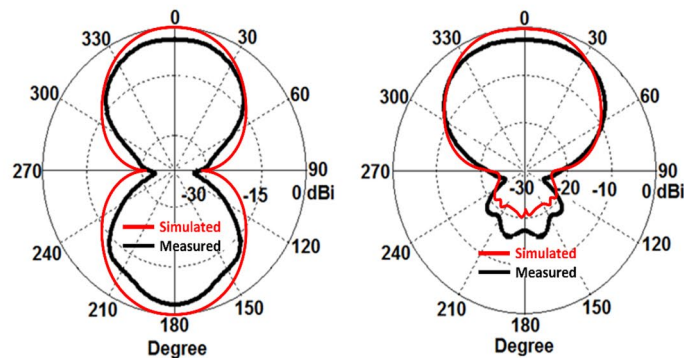
(i)

(j)

Fig. 4. (continued)

transfer. Finally, the slot-loaded radiation patches on the top surface further enhance the effective radiating area, improving beam directivity and overall radiation performance.

In Fig. 4g, the radiation efficiency exhibits a similar trend. The simulated efficiency is higher across the frequency range, reflecting the theoretical potential of the design. The experimental efficiency, while slightly lower, aligns closely with the simulation, demonstrating the antenna's high efficiency despite fabrication and measurement constraints. The average measured radiation efficiency across 25–30 GHz is 86.25%, validating the effectiveness of the slot-loaded design in achieving high gain and efficiency.

Discrepancies between simulated and measured radiation gain and efficiency can be attributed to fabrication tolerances, measurement conditions, and simulation assumptions. Real-world testing introduces external factors such as reflections, interference, and misalignment, which may impact measured performance. Additionally, cable and connector losses, as well as calibration errors, can further contribute to these differences. In contrast,

S-parameters	Initial antenna array	DGS loaded with CSRR	DGS loaded with CSRR and oblique slots	DGS loaded with CSRR, oblique slots and radiation patches loaded with a slot
Frequency bandwidth (GHz)	0.5 GHz (26–26.5) 0.5 GHz (27.5–28)	3.4 (25.35–28.75)	4.65 (25.35–30)	5 (25–30)
Fractional bandwidth (%)	1.90 & 1.80	12.56	16.80	18.18
Resonance Frequencies (f_r) (GHz)	26.25 & 27.75	25.75 & 27.7	26.30 & 28.70	26.0 & 28.25
Impedance matching at f_r (dB)	− 19 & − 12	− 15 & − 14	− 38 & − 30	− 40 & − 40
Average matching improvement over the initial array #1 (dB)	–	Unchanged	20	25
Average isolation between antennas #1 & #2 (S_{12}) (dB)	− 8	− 24	− 31	− 36
Average isolation between antennas #1 & #3 (S_{13}) (dB)	− 12	− 25	− 37	− 40
Average isolation between antennas #1 & #4 (S_{14}) (dB)	− 10	− 22	− 36	− 42
S_{12} improvement over initial array #1 (dB)	–	16	23	28
S_{13} improvement over initial array #1 (dB)	–	13	25	28
S_{14} improvement over initial array #1 (dB)	–	12	26	32

Table 2. S-parameter performance.

Antenna parameters	Initial antenna array (array #1)	DGS loaded with CSRR (array #2)	DGS loaded with CSRR and oblique slots (array #3)	DGS loaded with CSRR, oblique slots and radiation patches loaded with a slot (array #4)
Gain (dBi)	2–3.6 (average: 2.8)	7–8.5 (average: 7.75)	7.5–10.8 (average: 9.15)	10.8–14 (average: 12.4)
Average gain improvement over initial array #1 (dBi)	–	4.95	6.35	9.6
Efficiency (%)	49–63 (average: 56)	64–73.5 (average: 68.75)	75.5–81.5 (average: 79.5)	85–87.5 (average: 86.25)
Average efficiency improvement over initial array #1 (%)	-	12.75	23.5	30.25

Table 3. Radiation properties across 25 ghz and 30 GHz.

simulations rely on idealized models and controlled conditions, which do not fully capture real-world complexities.

The measurement setup and radiation characteristics of the antenna array is shown in Fig. 4h. The reference antenna was connected to the Vector Network Analyzer as the receiver, while the proposed antenna under test was connected to a signal source. The radiated power from the proposed antenna was measured at various angles to capture its radiation pattern. The measured radiation patterns of the optimized antenna array at 26 GHz and 28.25 GHz are shown in Fig. 4i, j for the E-plane and H-plane, respectively. At 26 GHz (Fig. 4i), the E-plane radiation pattern is symmetrical and bidirectional, with sharp nulls at 90° and 270°. The main lobes exhibit strong directivity, ensuring efficient radiation in the desired directions. The sidelobes remain minimal, indicating effective suppression of unwanted radiation. The H-plane pattern, while broader and slightly less symmetrical, maintains a well-defined main lobe, though minor ripples may be due to mutual coupling or structural imperfections. Overall, the pattern ensures stable radiation across a wide angular range.

At 28.25 GHz (Fig. 4j), the E-plane pattern remains bidirectional but exhibits slightly more pronounced sidelobes compared to 26 GHz. The main lobes remain well-directed, ensuring strong radiation performance. The H-plane pattern is broader than the E-plane, maintaining a consistent main lobe with slightly increased ripple effects. Despite minor variations, the overall radiation pattern remains stable, indicating robust array behavior at higher frequencies.

Across both frequencies, the optimized antenna array demonstrates effective radiation characteristics, with high directivity in the E-plane and broad, stable radiation in the H-plane. The low sidelobe levels and consistent main lobe behavior validate the array's optimized design for high-performance operation across the 25–30 GHz band. A summary of the performance characteristics of the four antenna array configurations is provided in Tables 2 and 3.

State-of-the-art comparison

The proposed MIMO antenna array demonstrates several key advantages over previously reported designs, which are listed in Table 4, in terms of gain, bandwidth, compactness, MIMO configuration, and fabrication simplicity. One of the most significant improvements is its higher gain performance, reaching 13.5 dBi, which surpasses all cited references. The closest alternative[22], achieves only 9.7 dBi, while others range between 6 dBi[23] and 10.5 dBi[24], highlighting the superior radiation efficiency of the proposed design. Higher gain directly translates to stronger signal transmission, improved coverage, and enhanced link reliability, making it particularly well-suited for 5G mm-Wave applications.

In addition to its impressive gain, the proposed antenna supports wideband operation at 26/28.25 GHz, covering critical frequency bands for 5G. While[25] also operates in a dual-band configuration (26/28 GHz), its

Ref.	Dimensions (mm³)	Frequency band (GHz)	Gain (dBi)	No. of arrays
22	4.8×2.9×0.762	26	9.7	2
23	20×18.9×0.5	27	6	2
24	75×75×0.6	28	10.5	4
25	45×3.2×1.4	26/28	7.3	1
26	50×15×0.2	28	10	1
27	10×18×0.508	28.8	6.5	4
28	20.5×12×0.79	28	8.1	2
Proposed work	32×32×0.8	26/28.25 GHz	13.5	4

Table 4. State-of-the-art comparison.

gain remains significantly lower at 7.3 dBi. Most other references operate at a single frequency, limiting their flexibility for multi-band applications. The proposed antenna's ability to function across multiple frequency bands ensures compatibility with diverse 5G use cases and future mm-Wave applications.

Despite its high performance, the proposed antenna maintains a compact and practical design, measuring $32 \times 32 \times 0.8$ mm³. While some cited references feature smaller dimensions, such as[22] ($4.8 \times 2.9 \times 0.762$ mm³), they compromise significantly on gain. On the other hand, larger designs like[24] ($75 \times 75 \times 0.6$ mm³) occupy more than four times the area but provide only 10.5 dBi of gain. The proposed antenna strikes a perfect balance between compactness and efficiency, making it an excellent choice for space-constrained 5G devices.

Another major advantage is the optimized MIMO configuration of the proposed antenna. Featuring a 4-element MIMO array, it enhances spatial diversity and mitigates multipath fading, significantly improving signal quality and data rates. In contrast, designs such as[23,25,26] use only 1 or 2 array elements, limiting their beamforming capabilities and overall performance. The 4-element configuration of the proposed design makes it highly effective in delivering enhanced throughput and reliable connectivity in demanding 5G environments.

Finally, the proposed antenna is cost-effective and easy to fabricate, owing to its Defected Ground Structure (DGS) with CSRRs, which enhances bandwidth and efficiency without requiring complex manufacturing techniques. Unlike SIW-based designs such as[27], which involve intricate feed structures and vias, the proposed antenna eliminates the need for complicated fabrication processes, making it more suitable for large-scale 5G deployment. The straightforward and scalable manufacturing process ensures that this antenna can be mass-produced efficiently without sacrificing performance.

Conclusion

MIMO antenna array designed for 5G millimeter-wave (mm-Wave) applications, effectively covering the 25–30 GHz frequency range. The proposed enhancements integrate multiple design techniques, including a Defected Ground Structure (DGS) with interlinked Complementary Split-Ring Resonator (CSRR) unit cells, DGS with oblique slots, and open-loop slot loading in the radiating elements. These techniques collectively improve the effective aperture, suppress surface wave losses, enhance impedance matching, and increase beam directivity, all without increasing the antenna's physical dimensions.

A key innovation in this design is the orthogonal arrangement of radiating elements, which significantly reduces electromagnetic coupling and enhances isolation between antenna ports. This is particularly important in dense antenna arrays, where unwanted coupling can degrade system performance. The proposed arrangement ensures high isolation, making the antenna array highly suitable for multi-port applications in 5G networks.

One of the most notable achievements of this work is that these performance improvements were achieved while maintaining a compact and practical form factor. With a footprint of $32 \times 32 \times 0.8$ mm³, the proposed design remains lightweight and easily integrable into modern 5G devices, where space constraints are critical.

Performance comparisons show that the proposed MIMO antenna array outperforms existing designs by offering the highest gain (13.5 dBi), broadband operation (26/28.25 GHz), and superior isolation while maintaining a cost-effective and scalable fabrication process. The use of DGS and CSRRs simplifies manufacturing, making the design well-suited for mass production and commercial deployment in next-generation wireless communication systems.

Furthermore, the proposed design is highly scalable and can be extended to larger antenna arrays, including massive MIMO configurations, without compromising size or efficiency. This scalability is crucial for future high-capacity, high-gain wireless communication systems, where beamforming and spatial diversity play a key role in enhancing data throughput and coverage. By demonstrating a practical and high-performance solution for compact MIMO antenna arrays, this research provides a strong foundation for the development of next-generation millimeter-wave antenna systems for 5G and beyond.

Data availability

All data generated or analyzed during this study are included in this published article.

References

1. Tantawy, Z. H., Mashade, M. B. E., Emran, M. B. A. A. & Semeia, A. I. On the performance of FSO communication system with WDM and MIMO structure under different turbulent atmospheric conditions. *J. Opt. Commun.*, **45**(s1), s2133–s2149 (2024).
2. Etman, A. M., Abdalzaher, M. S., Emran, A. A., Yahya, A. & Shaaban, M. A survey on machine learning techniques in smart grids based on wireless sensor networks. *IEEE Access.* **13**, 2604–2627 (2025).
3. Elsharief, M., Emran, A. A., Hassan, H., Sabuj, S. R. & Jo, H. S. SLES: Scheduling-Based Low Energy Synchronization for Industrial Internet of Things. *IEEE Sens. J.* **22**(16), 16652–16661 (2022).
4. Qasem, N. Measurement and simulation for improving indoor wireless communication system performance at 2.4 ghz by modifying the environment. *IEEE Access.* **12**, 96660–96671 (2024).
5. Rappaport, T. S. et al. Millimeter wave mobile communications for 5G cellular: it will work! *IEEE Access.* **1**, 335–349. https://doi.org/10.1109/ACCESS.2013.2260813 (2013).
6. Qasem, N. Exploring 60 ghz millimeter-wave indoor propagation path loss models and capacity enhancement for modified indoor environments. *J. Commun.* **19** (7), 340–349 (2024).
7. Andrews, J. G. et al. Jun., What will 5G be? *IEEE J. Sel. Areas Commun.* **32**(6), 1065–1082 (2014).
8. Qiao, J. et al. Enabling Device-To-Device communications in Millimeter-Wave 5G cellular networks. *IEEE Commun. Mag.* **53** (1), 209–215 (2015).
9. Huo, Y., Dong, X. & Xu, W. 5G Cellular User Equipment: From Theory to Practical Hardware Design, (2017). Available: http://arxiv.org/abs/1704.02540.
10. Roh, W. et al. Millimeter-Wave beamforming as an enabling technology for 5G cellular communications: theoretical feasibility and prototype results. *IEEE Commun. Mag.* **52** (2), 106–113 (2014).
11. Sethi, W. T., Ashraf, M. A., Ragheb, A., Alasaad, A. & Alshebeili, S. A. Demonstration of Millimeter Wave 5G Setup Employing High-Gain Vivaldi Array. *Int. J. Antennas Propag.* 3927153, 12. https://doi.org/10.1155/2018/3927153 (2018).
12. Stanley, M. et al. A High Gain Steerable Millimeter-Wave Antenna Array for 5G Smartphone Applications. In *2017 11th European Conference on Antennas and Propagation (EUCAP), Paris, France*, 2017, pp. 1311–1314. https://doi.org/10.23919/EuCAP.2017.7928542.
13. Ojaroudiparchin, N., Shen, M. & Pedersen, G. F. A 28 GHz FR-4 Compatible Phased Array Antenna for 5G Mobile Phone Applications. In *2015 International Symposium on Antennas and Propagation (ISAP)*, pp. 1–4, Hobart, TAS, Australia, (2015).
14. Gupta, S., Briqech, Z., Sebak, A. R. & Denidni, T. A. Mutual coupling reduction using metasurface corrugations for 28 ghz MIMO applications. *IEEE Antennas Wirel. Propag. Lett.* **16**, 2763–2766 (2017).
15. Chin, K. S. et al. 28-GHz Patch Antenna Arrays with PCB and LTCC Substrates. In *Proc. 2011 Cross Strait QuadRegional Radio Science and Wireless Technology Conf.*, pp. 355–358, Harbin, China, (2011).
16. Han, W., Yang, F., Ouyang, J. & Yang, P. Low-Cost wideband and High-Gain slotted cavity antenna using High-Order modes for Millimeter-Wave applications. *IEEE Trans. Antennas Propag.* **63** (11), 4624–4631 (2015).
17. Nor, N. M., Jamaluddin, M. H., Kamarudin, M. R. & Khalily, M. Rectangular dielectric resonator antenna array for 28 ghz applications. *Prog Electromagn. Res. C.* **63**, 53–61 (2016).
18. Online webpage. https://www.3ds.com/products/simulia/cst-studio-suite.
19. Alibakhshikenari, M. et al. A comprehensive survey of metamaterial Transmission-Line based antennas: design, challenges, and applications. *IEEE Access.* **8**, 144778–144808. https://doi.org/10.1109/ACCESS.2020.3013698 (2020).
20. Islam, M. T. et al. Metasurface loaded high gain antenna based microwave imaging using iteratively corrected delay multiply and sum algorithm. *Sci. Rep.* **9** (17317). https://doi.org/10.1038/s41598-019-53857-0 (2019).
21. Hoque, A. et al. A polarization independent Quasi-TEM metamaterial absorber for X and Ku band sensing applications. *Sensors* **18**, 4209 (2018).
22. Esmail, B. A. F. & Koziel, S. Design and optimization of metamaterialbased dual-band 28/38 ghz 5G MIMO antenna with modified ground for isolation and bandwidth improvement. *IEEE Antennas Wirel. Propag. Lett.* **22** (5), 1069–1073 (2023).
23. Gao, M. et al. A 2-Port high isolation millimeter wave Dual-Band antenna based on SIW back cavity slot. *Progress Electromagnet. Res. M*, **130**, (2024).
24. Baghel, N. & Mukherjee, S. SICL based multifunctional MIMO antenna array for 5G & beyond (B5G) applications. *IEEE Antennas. Wirel. Propag. Lett.* **23** (6), 1799–1803 (2024).
25. Liu, X., Zhang, W., Hao, D. & Liu, Y. Cost-Effective broadband and compact patch antenna based on ball grid array packaging for 5G NR FR2 band applications. *IEEE Trans. Circuits Syst. II Express Briefs.* **70** (6), 1921–1925 (2023).
26. Joseph, S. D. & Ball, E. A. Series-Fed Millimeter-Wave antenna array based on microstrip line structure. *IEEE Open. J. Antennas Propag.* **4**, 254–261 (2023).
27. Aboualalaa, M. & Mansour, I. Dual-band end-fire four-element MIMO antenna array using split-ring structure for mm-wave 5G applications. *IEEE Access.* **11**, 57383–57390 (2023).
28. Taher, F. et al. Design and analysis of circular polarized two-port MIMO antennas with various antenna element orientations. *Micromachines* **14** (2), 380 (2023).

Acknowledgements

Author contributions

Conceptualization, E.M.A., M.A., N.A.E., B.S.V., M.A.C., P.L., T.S.; methodology, E.M.A., M.A., N.A.E., B.S.V., N.R., N.A.A., P.L., T.S.; software, E.M.A., M.A., N.A.E., B.S.V.; validation, E.M.A., M.A., N.A.E., B.S.V., N.R., D.M., M.A.C., N.A.A., P.L., T.S.; formal analysis, E.M.A., M.A., N.A.E., B.S.V., N.R., M.A.C., T.S.; investigation, E.M.A., M.A., N.A.E., B.S.V., N.R., D.M., M.A.C., N.A.A.; resources, E.M.A., M.A., N.A.E., B.S.V., N.A.A., P.L.; data curation, E.M.A., M.A., N.A.E., B.S.V., M.A.C., N.A.A.; writing—original draft preparation, E.M.A., M.A.; writing—review and editing, E.M.A., M.A., N.A.E., B.S.V., N.R., D.M., M.A.C., N.A.A., P.L., T.S.; visualization, E.M.A., M.A., N.A.E., N.A.A.; supervision, M.A., T.S.; project administration, M.A., P.L.; funding acquisition, M.A., N.A.E., P.L. All authors have read and agreed to the published version of the manuscript.

Declarations

Competing interests
The authors declare no competing interests.

Additional information
Correspondence and requests for materials should be addressed to M.A., N.A.E. or P.L.

Reprints and permissions information is available at www.nature.com/reprints.

Publisher's note Springer Nature remains neutral with regard to jurisdictional claims in published maps and institutional affiliations.